CrossMark

J. Fluid Mech. (2019), *vol.* 873, *pp.* 238–259. © Cambridge University Press 2019
doi:10.1017/jfm.2019.428

Focusing deep-water surface gravity wave packets: wave breaking criterion in a simplified model

Nick Pizzo[1],† **and W. Kendall Melville**[1]

[1]Scripps Institution of Oceanography, University of California San Diego, La Jolla, CA 92037, USA

(Received 14 March 2018; revised 19 May 2019; accepted 21 May 2019; first published online 24 June 2019)

Geometric, kinematic and dynamic properties of focusing deep-water surface gravity wave packets are examined in a simplified model with the intent of deriving a wave breaking threshold parameter. The model is based on the spatial modified nonlinear Schrödinger equation of Dysthe (*Proc. R. Soc. Lond.* A, vol. 369 (1736), 1979, pp. 105–114). The evolution of initially narrow-banded and weakly nonlinear chirped Gaussian wave packets are examined, by means of a trial function and a variational procedure, yielding analytic solutions describing the approximate evolution of the packet width, amplitude, asymmetry and phase during focusing. A model for the maximum free surface gradient, as a function of ϵ and Δ, for ϵ the linear prediction of the maximum slope at focusing and Δ the non-dimensional packet bandwidth, is proposed and numerically examined, indicating a quasi-self-similarity of these focusing events. The equations of motion for the fully nonlinear potential flow equations are then integrated to further investigate these predictions. It is found that a model of this form can characterize the bulk partitioning of $\epsilon - \Delta$ phase space, between non-breaking and breaking waves, serving as a breaking criterion. Application of this result to better understanding air–sea interaction processes is discussed.

Key words: surface gravity waves, wave breaking

1. Introduction

This investigation is concerned with initially narrow-banded and weakly nonlinear chirped compact deep-water wave groups and their evolution towards wave breaking. A distinguishing characteristic of these focusing packets is shown in figure 1, where packet asymmetry is manifest, and the packet slope reaches large negative values, resulting in wave breaking. The central question of this study is, which mechanisms control this behaviour in focusing nonlinear wave packets? To quantify this a dimensionless parameter, $\mathcal{T} = \mathcal{T}(\epsilon, \Delta)$, for ϵ a measure of the linear prediction of the maximum wave slope at focusing and Δ the dimensionless packet bandwidth, is proposed as a prediction of the local wave slope. When this parameter exceeds a certain threshold, wave breaking is expected.

†Email address for correspondence: npizzo@ucsd.edu

https://doi.org/10.1017/jfm.2019.428 Published online by Cambridge University Press

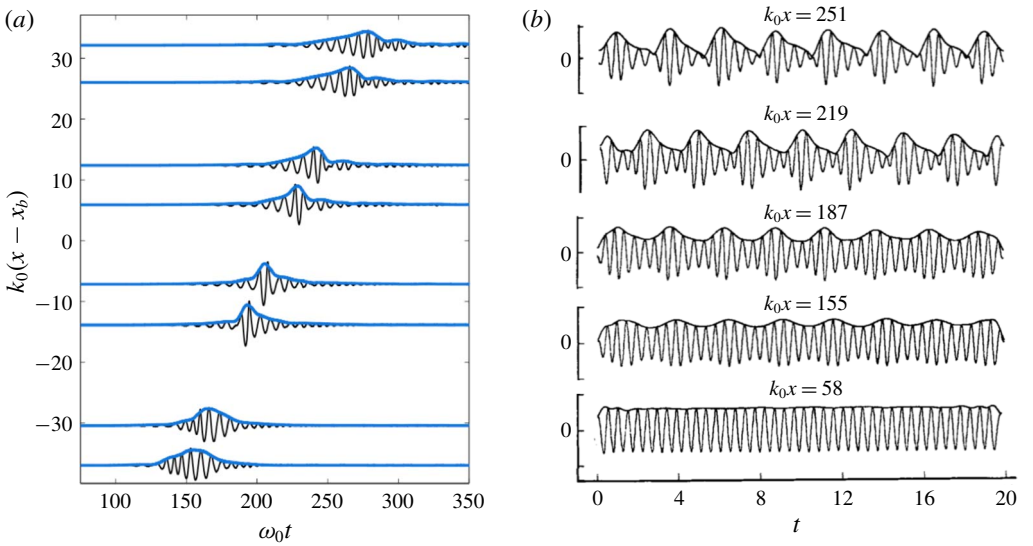


FIGURE 1. (Colour online) Two laboratory examples of deep-water breaking waves. (*a*) Laboratory data from Drazen, Melville & Lenain (2008). A dispersive focusing technique is employed to create breaking around $k_0(x - x_b) = 0$. The wave envelope is shown in blue, while the free surface displacement is given in black. Notice the strong asymmetry in the packet as breaking is approached. (*b*) The evolution of an initially uniform train of finite amplitude waves, from the laboratory experiments of Melville (1983). The initially uniform wave train experiences the Benjamin–Feir instability (Benjamin & Feir 1967), leading to large modulations to the wave amplitude and phase, eventually leading to wave breaking around $k_0x = 251$.

Recently, physically motivated scaling arguments have been successful in describing bulk scale properties of the flow induced by deep-water wave breaking. For example, consider the energy dissipation rate due to deep-water breaking waves (Duncan 1981; Phillips 1985; Drazen *et al.* 2008; Romero, Melville & Kleiss 2012; Sutherland & Melville 2013; Deike, Popinet & Melville 2015). Drazen *et al.* (2008) found that the dissipation rate per unit length of length of breaking crest is given by $b_0(S - S_0)^{5/2}\rho c^5/g$ for b_0 a scaling constant, S the linear prediction of the maximum wave slope at focusing, ρ the density of water, c the phase velocity, g the acceleration due to gravity and S_0 is the breaking threshold. Part of the motivation of this manuscript is to better understand this threshold quantity S_0. For instance, does it depend on other quantities characterizing the wave packet such as the bandwidth? Improved understanding of the behaviour of this threshold may then be used to further constrain the scaling arguments that are used to close energy budgets between the atmosphere and ocean (Cavaleri, Fox-Kemper & Hemer 2012; Sutherland & Melville 2015), and may be incorporated into wave models to parametrize the wave breaking statistics (Phillips 1985) in studies of air–sea interaction (Sullivan, McWilliams & Melville 2007).

In this paper we employ the spatial modified nonlinear Schrödinger equation (hereinafter referred to as the MNLSE; Dysthe 1979; Lo & Mei 1985). The model is weakly nonlinear and narrow banded. How then may it be useful in describing wave breaking, which is a process that is very nonlinear (with the local free surface slope potentially going to negative infinity) and varies rapidly in space

https://doi.org/10.1017/jfm.2019.428 Published online by Cambridge University Press

and time? Our approach is to distinguish physical mechanisms, and in particular bulk scale non-dimensional quantities describing these mechanisms, that characterize the magnitude of the gradients of the free surface displacement generated from initially narrow-banded weakly nonlinear wave packets. Here, using the variational method (Chandrasekhar 2013, §17) for an asymmetric trial function following Pizzo & Melville (2016, see also Anderson 1983), solutions for the packet amplitude, asymmetry, width and phase are found. A condition is derived, as a function of a non-dimensional number, under which the packet slope experiences large amplifications, implying its potential usefulness in quantifying the strength of packet focusing. Furthermore, the analysis hints at a quasi-self-similarity in the behaviour of the maximum slope in these focusing wave packets. Note, the mechanisms generating these large free surface displacement gradients are not directly responsible for wave breaking but may instead trigger higher-order local crest instabilities (e.g. the five wave resonance of steep waves (discussed in more detail below), see Longuet-Higgins 1978; McLean *et al.* 1981; Longuet-Higgins & Dommermuth 1997). Subsequently, this analysis is examined by integrating the fully nonlinear potential flow equations. Despite the limitations of the MNLSE (which have been elucidated in a number of laboratory and numerical experiments, see for instance Lo & Mei (1985), Shemer, Kit & Jiao (2002), Clamond *et al.* (2006)), due to the complexity of the full problem (Perlin, Choi & Tian 2013), there is insight gained by examining a minimal model that reproduces features that are observed in laboratory, numerical, and field observations of breaking waves.

Wave breaking in deep water may occur due to wave–wave interactions, wave–current interactions and wind–wave interactions (Melville 1996). In this study, we are particularly interested in wave breaking due to wave–wave interactions so that we do not consider the effects of winds or external currents. Wave breaking has been studied theoretically since Stokes proposed the limiting form of permanent progressive waves (Stokes 1880, see also Craik 2005). Mathematically, breaking is often identified with shock formation (Seliger 1968; Whitham 1974) or divergences in measures of the packet variance, as is common in virial theorem arguments for the nonlinear Schrödinger equation and its variants (Sulem & Sulem 1999). For permanent progressive waves, five wave and higher resonances of very steep Stokes waves may rapidly lead to wave overturning (Longuet-Higgins & Dommermuth 1997), corresponding to a homoclinic bifurcation (Bridges 2004), but these waves tend to be of limited interest in practice due to their restriction to infinitesimal bandwidth. Although there has been significant theoretical and practical advances in our understanding of deep-water wave breaking, the principles guiding breaking are not fully known, making diagnostic and predictive modelling of a breaking threshold difficult (Perlin *et al.* 2013). Furthermore, it is not clear which variables describing the wave field are needed to characterize this behaviour.

Laboratory observations have been particularly successful in advancing our understanding of wave breaking. Two different generation mechanisms that lead to breaking are the evolution of an initially permanent progressive finite amplitude wave train to breaking (Melville 1982, 1983) and a dispersive focusing technique (Melville & Rapp 1985; Rapp & Melville 1990) originally proposed by Longuet-Higgins (1974). Breaking in both instances is shown in figure 1, where both amplitude amplification and a strong asymmetry in the packet envelope is evident.

Next, Dyachenko & Zakharov (2011) derived an equation that is accurate to fourth order in wave slope, under the additional constraint that waves are travelling in one direction. Under these conditions, they derived a compact equation that is not

https://doi.org/10.1017/jfm.2019.428 Published online by Cambridge University Press

limited by bandwidth constraints. Fedele (2014) then used this equation to examine the evolution of an initially uniform very steep wave train (there the slope exceeds 0.577, while we recall the limiting Stokes wave has slope of around 0.443 (Stokes 1880)), where the envelope amplitude and wavenumber evolution was hyperbolic, and derived a modified Camassa–Holm equation (Camassa & Holm 1993) governing the envelope evolution, which admits breaking. Dyachenko, Kachulin & Zakharov (2017) also used this equation to examine steepening waves. However, breaking criterion and comparisons against the fully nonlinear potential flow equations were not provided, and it is not clear how accurate these descriptions are when applied so far outside of their asymptotic region of validity. Furthermore, the canonical transformations of the Zakharov equation needed to derive these equations (Dyachenko & Zakharov 2011) partially obscure the physics of these results.

Recently, Barthelemy *et al.* (2018) proposed, and Saket *et al.* (2017, see also Khait & Shemer 2018) provided laboratory support for, a kinematic criterion for wave breaking (Perlin *et al.* 2013), providing a diagnostic tool to locally analyse the likelihood of breaking. The connection between this local kinematic behaviour and the initial conditions of dispersive focusing packets (which are characterized by linear predictions of their geometry at focusing) partially motivated this study. Note, power law behaviour of certain properties of breaking waves, such as length scales near breaking, have been examined theoretically in Pomeau *et al.* (2008), but this study diagnoses the behaviour of the waves once breaking has taken place, and does not present a criterion nor a mechanism for breaking to occur.

The outline of this paper is as follows. In § 2, the modified nonlinear Schrödinger equation is reviewed. Next, in § 3, the evolution of initially narrow-banded weakly nonlinear chirped Gaussian packets is considered. A model is proposed to predict the maximum wave slope at focusing. The theory is then examined numerically in the fully nonlinear irrotational inviscid system in § 4. Finally, the results are discussed in § 5.

2. The modified nonlinear Schrödinger equation

In this section we review properties of the modified nonlinear Schrödinger equation (Dysthe 1979), in a spatially mapped reference frame (Lo & Mei 1985). This follows Pizzo & Melville (2016), and we note that a more general description of the Hamiltonian form of Dysthe's equation may be found in Gramstad & Trulsen (2011, see also Kit & Shemer (2002)).

2.1. *Derivation of the MNLSE using Whitham's method*

The governing equation for irrotational inviscid two dimensional surface gravity waves is (see, for example, Phillips 1977)

$$\nabla'^2\phi' = 0, \tag{2.1}$$

together with boundary conditions

$$\phi'_{t'} + \tfrac{1}{2}(\boldsymbol{\nabla}'\phi')^2 + gz' = 0\big|_{z'=\eta'}; \quad \eta'_{t'} + \phi'_{x'}\eta'_{x'} = \phi'_{z'}\big|_{z'=\eta'}, \tag{2.2a,b}$$

along with the condition of no flow at the bottom $\phi'_{z'} \to 0$ as $z' \to -\infty$, where ϕ' is the velocity potential, η' is the free surface displacement, $\boldsymbol{\nabla}' = (\partial_{x'}, \partial_{z'})$ and g is the acceleration due to gravity. Although the governing equation is linear, the boundary

https://doi.org/10.1017/jfm.2019.428 Published online by Cambridge University Press

conditions are nonlinear, and more severely, are evaluated at a dependent variable of the system, namely η'.

In order to make analytic progress, asymptotic approximations are employed. The wave slope $\epsilon \equiv a_0 k_0$ is a measure of the nonlinearity of the system, and is assumed to be much less than 1. Furthermore, if δk is a perturbation to the characteristic wavenumber k_0, then we define the bandwidth as $\Delta \equiv |\delta k|/k_0$. Now, unlike the canonical approach where $\Delta \sim \epsilon$, we instead leave the exact relationship between the two parameters general (see also the discussion in Phillips (1981)). Finally, the characteristic angular frequency, ω_0, is related to the wavenumber by the linear dispersion relation for deep water surface gravity waves, i.e. $\omega_0^2 = g k_0$.

Following (Lo & Mei 1985), we non-dimensionalize our system as follows:

$$\left.\begin{aligned} \phi = (a_0^2\omega_0)^{-1}\phi', \quad \eta = a_0^{-1}\eta', \\ x = k_0 x', \quad t = \omega_0 t', \quad z = k_0 z'. \end{aligned}\right\} \tag{2.3}$$

Expanding the velocity potential and free surface displacement as a series, we have (Chu & Mei 1970)

$$\phi = \overline{\phi}(X, T; \epsilon, \Delta) + \sum_{l=1}^{M}\sum_{m=1}^{M}\sum_{n\geqslant m}^{N} \epsilon^{n-1}\Delta^{l-1}\phi_{lmn}(X, T, Z)\mathrm{e}^{\mathrm{i}m\theta}\mathrm{e}^{mz} + \text{c.c.}, \tag{2.4}$$

$$\eta = \overline{\eta}(X, T; \epsilon, \Delta) + \sum_{l=1}^{M}\sum_{m=1}^{M}\sum_{n\geqslant m}^{N} \epsilon^{n-1}\Delta^{l-1}\eta_{lmn}(X, T)\mathrm{e}^{\mathrm{i}m\theta} + \text{c.c.}, \tag{2.5}$$

where $X = \Delta x$, $Z = \Delta z$, $T = \Delta t$, $\theta = x - t$ and c.c. means complex conjugate; $\overline{\phi}$ and $\overline{\eta}$ are the mean (phase-averaged) velocity potential and free surface displacement, respectively, with their scale to be determined. Finally, we take the complex valued coefficient $\phi_{111} \equiv B$ as our dependent variable. This has important implications for the structure of the resulting governing equation (see the discussion in Kit & Shemer (2002) and Trulsen (2006)).

The expansions of the dependent variables to third order in ϵ and second order in Δ, appropriate for the MNLSE, are (Trulsen & Dysthe 1997; Trulsen 2006; Pizzo & Melville 2016)

$$\phi = \epsilon\overline{\phi} + \frac{1}{2}\left(\left[B - \mathrm{i}\Delta z B_X - \frac{\Delta^2}{2}z^2 B_{XX}\right]\mathrm{e}^{z}\mathrm{e}^{\mathrm{i}\theta} + \text{c.c.}\right), \tag{2.6}$$

$$\begin{aligned} \eta \;=\; & \epsilon\Delta\overline{\eta} + \frac{1}{2}\left(\left[\mathrm{i}B + \frac{\Delta}{2}B_X + \frac{\mathrm{i}\Delta^2}{8}B_{XX} + \frac{\mathrm{i}\epsilon^2}{8}|B|^2 B\right]\mathrm{e}^{\mathrm{i}\theta}\right. \\ & \left. + \left[-\frac{\epsilon}{2}B^2 + \mathrm{i}\epsilon\Delta B B_X\right]\mathrm{e}^{2\mathrm{i}\theta} + \frac{3\mathrm{i}\epsilon^2}{8}B^3\mathrm{e}^{3\mathrm{i}\theta} + \text{c.c.}\right). \end{aligned} \tag{2.7}$$

Recall, equations (2.1), (2.2) can be reformulated in terms of a variational principle through the action (Luke 1967; Zakharov 1968; Miles 1977)

$$\int L\,\mathrm{d}x\,\mathrm{d}t = \int\left\{\epsilon\psi\eta_t - \epsilon\left(\int_{-\infty}^{\epsilon\eta}\frac{1}{2}(\nabla\phi)^2\,\mathrm{d}z + \frac{1}{2}\eta^2\right)\right\}\mathrm{d}x\,\mathrm{d}t, \tag{2.8}$$

where $\psi = \phi(x, z = \epsilon\eta, t)$ is the velocity potential evaluated at the free surface.

https://doi.org/10.1017/jfm.2019.428 Published online by Cambridge University Press

Next, we substitute the form of the velocity potential and free surface displacement into (2.8). Furthermore, following Lo & Mei (1985), we map into a spatial reference frame by introducing the following transformation

$$(2X - T) = \tau; \quad \Delta X = \chi. \tag{2.9a,b}$$

This reference frame is travelling at the linear group velocity, and for a fixed position X, τ is proportional to the negative of the elapsed time, while χ is related to the fetch (or stretched distance). Finally, for clarity of presentation we transform from the dependent variable B to the dependent variable in the mapped frame A.

Employing the mapping given by (2.9), the averaged Lagrangian (Whitham 1965, 1974), then becomes

$$\mathcal{L} \equiv \frac{1}{2\pi}\int_0^{2\pi} L\,\mathrm{d}\theta = \frac{\mathrm{i}}{2}\left(A\frac{\partial A^*}{\partial \chi} - A^*\frac{\partial A}{\partial \chi}\right) - \mathcal{H}, \tag{2.10}$$

where $\mathcal{H}$ is defined as (cf. Gramstad & Trulsen 2011, appendix C)

$$\mathcal{H} = |A_\tau|^2 - \frac{\gamma_0}{2}|A|^4 - \frac{\alpha_0}{2}|A|^2\mathbb{H}(|A|_\tau^2) + \mathrm{i}\frac{\beta_0}{4}|A|^2(A^*A_\tau - AA_\tau^*), \tag{2.11}$$

and $\gamma_0 = \epsilon^2/\Delta^2$, $\alpha_0 = 2\epsilon^2/\Delta$, $\beta_0 = 8\epsilon^2/\Delta$, while * denotes the complex conjugate. Note, γ_0 is a measure of the ratio of the $O(\epsilon^2)$ nonlinearity to dispersion (this term has been shown to be important for statistical analogues of the NLSE (Alber 1978; Onorato *et al.* 2001; Janssen 2003) as well as the deterministic dynamics of the NLSE (Anderson 1983)) and the Hilbert transform $\mathbb{H}$ is defined as

$$\mathbb{H}(|A|_\tau^2) = \frac{1}{\pi}P.V.\int_{-\infty}^{\infty}\frac{\partial|A(\chi,\tau')|^2}{\partial\tau'}\frac{\mathrm{d}\tau'}{\tau-\tau'}, \tag{2.12}$$

with $P.V.$ meaning we are to take the principal value of the integral (Titchmarsh 1948). Following Janssen (1983, see also Akylas 1989) we have rewritten our action in terms of one variable by recognizing that $\overline{\varphi_\tau}$ and $\overline{\varphi_Z}$ are harmonic conjugates, where φ is the velocity potential in this spatial reference frame. That is, these variables are real and imaginary parts of an analytic function in the lower half plane and hence we can connect the two variables, evaluated at $Z = 0$, via the Hilbert transform $\mathbb{H}$.

As the linear dispersion is exactly represented in this spatial reference frame (Trulsen *et al.* 2000; Kit & Shemer 2002), only one term is needed to completely describe it. Besides making this equation more physically accurate, this also offers numerical advantages (Lo & Mei 1985), and simplifies the equations algebraically.

The action associated with the Lagrangian density in the spatial reference frame, i.e. equation (2.10), is defined as

$$\mathcal{S}(A, A^*) = \int_{\chi_0}^{\chi_f}\int_{\mathbb{R}}\mathcal{L}\,\mathrm{d}\tau\,\mathrm{d}\chi, \tag{2.13}$$

which is a functional over all admissible functions satisfying the prescribed conditions at $A(\tau, \chi_0)$ and $A(\tau, \chi_f)$. Hamilton's principle states that the governing equations of the system are found by requiring that $\mathcal{S}$ be stationary. That is, we seek solutions (A, A^*) such that

$$\delta\mathcal{S} = \mathcal{S}(A + \delta A, A^* + \delta A^*) - \mathcal{S}(A, A^*) = 0, \tag{2.14}$$

https://doi.org/10.1017/jfm.2019.428 Published online by Cambridge University Press

for infinitesimal $(\delta A, \delta A^*)$. Substituting the Lagrangian density into the action, then applying Hamilton's principle, and recalling the anti-self-adjoint nature of the Hilbert transform (Titchmarsh 1948), gives us (Lo & Mei 1985; Kit & Shemer 2002)

$$\frac{\partial A}{\partial \chi} + \mathrm{i}\frac{\partial^2 A}{\partial \tau^2} + \mathrm{i}\gamma_0 |A|^2 A + \mathrm{i}\alpha_0 A \mathbb{H}\left(\frac{\partial |A|^2}{\partial \tau}\right) + \beta_0 |A|^2 \frac{\partial A}{\partial \tau} = 0. \tag{2.15}$$

The constants (α_0, β_0) also make it easy to track the induced mean flow (which is related to the term with coefficient α_0), and the asymmetric self-steepening term (which is related to the term with coefficient β_0) in the ensuing calculations. Note, for $\Delta = \epsilon$, we return the standard form of the MNLSE.

This equation is usually written as a set of coupled partial differential equations (PDEs) in two dependent variables, $(A, \overline{\varphi}|_{Z=0})$. The two variables are connected by the relation

$$\left.\frac{\partial \overline{\varphi}}{\partial Z}\right|_{Z=0} = \frac{\partial |A|^2}{\partial \tau}, \tag{2.16}$$

which implies that gradients in the radiation stress lead to the generation of a mean flow (Longuet-Higgins & Stewart 1964; Dysthe 1979; McIntyre 1981).

2.2. *Conservation laws*

A benefit of the above use of Whitham's method is that symmetries of the action (2.13) may be connected with conservation laws using Noether's theorem. In particular, Pizzo & Melville (2016) were able to identify several symmetries of the action of the Lagrangian associated with (2.15). They found that (2.15) conserves wave action,

$$\frac{\partial |A|^2}{\partial \chi} + \frac{\partial}{\partial \tau}\left(\mathrm{i}(A^* A_\tau - A A_\tau^*) + \frac{\beta_0}{2}|A|^4\right) = 0, \tag{2.17}$$

as well as the wave action weighted frequency (Trulsen & Dysthe 1997)

$$\frac{\partial}{\partial \chi}(\mathrm{i}(A^* A_\tau - A A_\tau^*)) + \frac{\partial \mathcal{G}}{\partial \tau} + 2\alpha_0 |A|_\tau^2 \mathbb{H}(|A|_\tau^2) = 0, \tag{2.18}$$

where

$$\mathcal{G} = 2|A_\tau|^2 - (A A_{\tau\tau}^* - A^* A_{\tau\tau}) - \gamma_0 |A|^4 + \mathrm{i}\beta_0 |A|^2 (A^* A_\tau - A A_\tau^*) - 2\alpha_0 |A|^2 \mathbb{H}(|A|_\tau^2). \tag{2.19}$$

As was noted in Pizzo & Melville (2016), equation (2.18) does not take the form of a local conservation law due to the last term in (2.18), which cannot be written as a perfect derivative. However, the integral quantity $\int \mathrm{i}(A^* A_\tau - A A_\tau^*)\,\mathrm{d}\tau$ is still conserved, as the final term on the left-hand side of (2.18) integrates to zero due to the anti-self-adjoint nature of the Hilbert transform (Titchmarsh 1948).

3. Focusing wave packets

The goal of this section is to identify non-dimensional parameters that characterize wave focusing as governed by (2.15). In the absence of a canonical structure to analyse for focusing wave packets, we must come up with a rational way to analytically examine the evolution of this system. To this end, following work in

https://doi.org/10.1017/jfm.2019.428 Published online by Cambridge University Press

fluid mechanics (Chandrasekhar 2013) and optics (Agrawal 2007), ansätze are made for a trial function and a variational method is used to determine its evolution.

Theoretically, we consider chirped, initially narrow-banded and weakly nonlinear, Gaussian wave packets. These waves are similar to the dispersive focusing wave packets originally proposed by Longuet-Higgins (1974) and used extensively in laboratory experiments on breaking waves (Melville & Rapp 1985; Rapp & Melville 1990; Tian, Perlin & Choi 2010; Perlin *et al.* 2013). Longer (faster) waves are generated after shorter (slower) waves, leading to energy focusing in a region of space and time, possibly leading to breaking.

Chirped Gaussian wave packets satisfying the linear Schrödinger (i.e. $\gamma_0{=}\alpha_0{=}\beta_0{=}0$) take the form

$$A = \frac{h_0}{\sqrt{1-2\mathrm{i}\Lambda\chi}}\mathrm{e}^{-\Lambda\tau^2/2(1-2\mathrm{i}\Lambda\chi)}, \tag{3.1}$$

where $\Lambda = (1+\mathrm{i}C)w^{-2}$, for C the packet chirp, and w the packet width. The packet bandwidth then scales with $w|\Lambda| = \sqrt{1+C^2}w^{-1}$ (Agrawal 2007).

3.1. *Variational equations*

Following Pizzo & Melville (2016), we use the variational method (Anderson 1983; Agrawal 2007; Chandrasekhar 2013), to derive approximate analytic forms for the evolution of physically important packet parameters. This qualifies and quantifies the packet evolution, and forms a useful tool to understand the bulk scale properties of the wave envelope during focusing. The success of this approach relies on a trial function which captures the essence of the phenomenon in question, without being too algebraically complicated.

To this end, we recall that in the absence of linear dispersion, as was discussed by Pizzo & Melville (2016), equations (2.17) and (2.18) decouple, and may be solved using the method of characteristics. For small $\beta_0\rho^2\chi$, solutions to the wave action equation (i.e. (2.17)) takes the form

$$\rho \approx \rho_0 + \beta_0\rho_0^2\rho_0'\chi, \tag{3.2}$$

where the subscript 0 means we are evaluating these functions at $\chi = 0$.

This implies that that for an initially chirped Gaussian wave packet, we should try a trial function of the form (Anderson 1983)

$$\mathcal{A} = (a(\chi)\mathrm{e}^{-\tau^2/2w(\chi)^2} + \beta_0 s(\chi)\tau\mathrm{e}^{-3\tau^2/2w(\chi)^2})\mathrm{e}^{\mathrm{i}(C(\chi)\tau^2/2+G(\chi)+\beta_0F(\chi)\tau)}, \tag{3.3}$$

where we are solving for the six real functions (a, s, w, C, F, G), governing the amplitude of the symmetric component of the packet a, the asymmetric amplitude s, the packet width w, the chirp C, the mean frequency F and the phase shift G.

To employ the variational technique we then substitute our trial wave function into the action, i.e. (2.13), so that to the same order of approximation as (2.15), we find

$$\mathfrak{L} = \int_{-\infty}^{\infty} L\,\mathrm{d}\tau = \sqrt{\frac{2}{\pi}}\alpha_0\varkappa_0a^4 - \sqrt{2}\frac{a^2}{w} + \gamma_0a^4w \tag{3.4}$$

$$- \sqrt{2}a^2C^2w^3 + \frac{a^2w^3C'}{\sqrt{2}} + 2\sqrt{2}a^2wG', \tag{3.5}$$

https://doi.org/10.1017/jfm.2019.428 Published online by Cambridge University Press

where $\varkappa_0$ is a constant given by

$$\varkappa_0 = \int_{-\infty}^{\infty} \mathrm{e}^{-(\tau/w)^2} \mathbb{H}((\mathrm{e}^{-(\tau/w)^2})_\tau)\,\mathrm{d}\tau = 1, \tag{3.6}$$

as the Hilbert transform of the Gaussian function may be written in terms of the Dawson function (Temme 2010), so that this integral may be computed analytically.

We begin by noting that the integral form of conservation of wave action, i.e. equation (2.17), becomes

$$E_0 = \int_{-\infty}^{\infty} |A|^2\,\mathrm{d}\tau = \sqrt{\pi} a^2 w + O(\beta_0^2), \tag{3.7}$$

where E_0 is a specified constant (independent of the scales ϵ and Δ) based on the initial wave form. Furthermore, conservation of mean frequency, i.e. the integral of (2.18), gives

$$P_0 = \frac{\mathrm{i}}{E_0} \int_{-\infty}^{\infty} (A^* A_\tau - A A_\tau^*)\,\mathrm{d}\tau = \frac{aw\beta_0}{8} \left(aF + \frac{Csw^2}{2\sqrt{2}} \right), \tag{3.8}$$

which for the initially chirped Gaussian function (3.1) must be taken to be zero, so that

$$F = -\frac{1}{2\sqrt{2}} \frac{sw^{5/2} C}{E_0^{1/2}}. \tag{3.9}$$

We can now apply Hamilton's principle to each of the dependent variables, yielding a set of coupled ordinary differential equations. Taking variations with respect to w implies

$$G' + \frac{3}{4} w^2 C' - \frac{3}{2} C^2 w^2 + \frac{1}{2w^2} + \frac{\gamma_0 a^2}{2\sqrt{2}} = 0, \tag{3.10}$$

while variations with respect to G gives

$$(a^2 w)' = 0, \tag{3.11}$$

which is consistent with equation (3.7).

Next, varying $\mathfrak{L}$ with respect to a we find

$$G' + \frac{1}{4} w^2 C' - \frac{1}{2} C^2 w^2 + \frac{\alpha_0 a^2}{\sqrt{\pi} w} - \frac{1}{2w^2} + \gamma_0 \frac{a^2}{\sqrt{2}} = 0, \tag{3.12}$$

while variations with respect to C yields

$$4a^2 w^3 C + (a^2 w^3)' = 0. \tag{3.13}$$

Next, recall Pizzo & Melville (2016) found that the centroid of packets governed by the MNLSE, in the frame of reference moving at the linear group velocity, have a finite amplitude correction analogous to the Stokes correction for permanent progressive waves. There, it was found that (for $P_0 = 0$)

$$\frac{\mathrm{d}}{\mathrm{d}\chi} \frac{1}{E_0} \int_{-\infty}^{\infty} \tau |A|^2\,\mathrm{d}\tau = \frac{\beta_0}{2E_0} \int_{-\infty}^{\infty} |A|^4\,\mathrm{d}\tau. \tag{3.14}$$

https://doi.org/10.1017/jfm.2019.428 Published online by Cambridge University Press

Substituting our trial function into this equation, we find a relationship for s,

$$s' + \frac{5}{2}\frac{w'}{w}s = \frac{8E_0^{3/2}}{w^{7/2}}. \tag{3.15}$$

Next, from equation (3.7), equation (3.13) can be rewritten to find

$$C = -\frac{1}{2}\frac{w'}{w} = -\frac{1}{2}\frac{\mathrm{d}\ln w}{\mathrm{d}\chi}. \tag{3.16}$$

Then, subtracting (3.10) from (3.12) and substituting in (3.16), we have

$$w'' + \gamma_0 E_0\sqrt{\frac{2}{\pi}}\frac{1}{w^2} + 4\left(-1 + \frac{\alpha_0 E_0}{\pi}\right)\frac{1}{w^3} = 0. \tag{3.17}$$

Multiplying by w' and integrating once, we find an equation describing a particle trapped in a potential well,

$$\frac{1}{2}\left(\frac{\mathrm{d}w}{\mathrm{d}\chi}\right)^2 + \Pi(w) = 0, \tag{3.18}$$

where the potential $\Pi(w)$ is given by

$$\Pi(w) = 2\left(1 - \frac{\alpha_0 E_0}{\pi}\right)\frac{1}{w^2} - \sqrt{\frac{2}{\pi}}\frac{\gamma_0 E_0}{w} + \Pi_0, \tag{3.19}$$

and Π_0 is an integration constant chosen to satisfy the initial conditions, that is

$$\Pi_0 = -1/2w_0'^2 - 2\left(1 - \frac{\alpha_0 E_0}{\pi}\right)\frac{1}{w_0^2} + \sqrt{\frac{2}{\pi}}\frac{\gamma_0 E_0}{w_0}. \tag{3.20}$$

The initial velocity of the particle in the well is set by the chirp of the packet and the initial width, as is evident by (3.16). Equation (3.19) makes it clear that the dynamics of w is set by the size of $(\epsilon/\Delta)^2$ and ϵ^2/Δ. Note, throughout the rest of this discussion we take E_0 to be $\sqrt{\pi}$, so that $a_0^2 w_0 = 1$.

Examples of potentials for two values of ϵ^2/Δ are shown in figure 2. There, the black dot represents the initial packet width (taken to be $w_0 = 1$). We take $C_0 < 0$ so that the packet width w decreases, leading to focusing. For increasing values of ϵ^2/Δ, this focusing event becomes more pronounced as linear dispersion is retarded by the induced mean flow.

The packet width may be solved for implicitly, as we may rewrite (3.18) as

$$\sqrt{2}\chi = \int_1^w \frac{\tilde{w}\mathrm{d}\tilde{w}}{\sqrt{-\tilde{w}^2\Pi_0 + \sqrt{2}\gamma_0\tilde{w} - 2(1 - \alpha_0/\sqrt{\pi})}}. \tag{3.21}$$

Next, equation (3.15) may be integrated to find

$$s = \frac{8E_0^{3/2}}{w^{5/2}}\int \frac{\mathrm{d}\tilde{\chi}}{w(\tilde{\chi})}. \tag{3.22}$$

The solutions to these equations are discussed in more detail below.

https://doi.org/10.1017/jfm.2019.428 Published online by Cambridge University Press

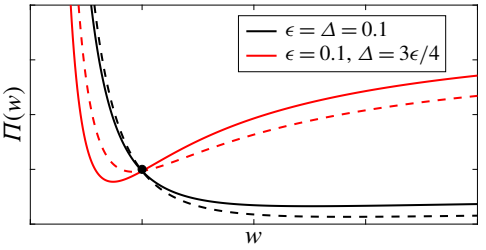


FIGURE 2. (Colour online) The potential well given by (3.19) for $\epsilon = \Delta = 0.1$ (black line) and $\epsilon = 4\Delta/3 = 0.1$ (red line). The dashed lines show the corresponding potentials for the nonlinear Schrödinger equation. Note, the red line has $\Pi'(w_0 = 1) < 0$, implying the nonlinearity is stronger than the dispersion initially, aiding the chirp in compressing the packet, i.e. leading to smaller values of w.

3.2. *Discussion*

The role of the individual terms in the MNLSE in modulating the focusing process is made clear by analysis done in § 3.1. From (3.19), we see that the role of the nonlinear term with coefficient γ_0 is to increase attraction, leading to larger focusing than if it were not present. At small w, the term proportional to w^{-2} dominates. There, the induced mean flow term, i.e. the term with coefficient α_0, counteracts linear dispersion. Furthermore, the connection between the asymmetric self-steepening term and the packet width is elucidated by (3.22). For w constant we return the prediction of Burgers equation, where it is found that for χ small, this asymmetric term grows linearly in χ. In the MNLSE, the changing packet width greatly modifies the growth rate of the asymmetric component (see (3.22)), and is extremely sensitive to this value, leading to large amplifications in this asymmetric amplitude.

The solutions to (3.21) are qualitatively controlled by the sign of $\Pi'(w_0)$ (which is evident by looking at the last two terms in (3.17)), which indicates whether dispersion or nonlinearity is dominant. Focusing is always possible based on the sign and magnitude of the initial chirp, but for $\Pi'(w_0) < 0$, we expect that nonlinearity is initially stronger than dispersion and this greatly enhances the focusing event. Figure 2 shows the potential wells for the NLSE and MNLSE for these two cases.

In particular, $\Pi'(w_0 = 1)$ changes sign when

$$\epsilon > 2\left(\frac{\sqrt{2}}{\Delta^2} + \frac{8}{\sqrt{\pi}\Delta}\right)^{-1/2} = \frac{2\pi^{1/4}\Delta}{\sqrt{\sqrt{2\pi} + 8\Delta}}. \tag{3.23}$$

For $\epsilon = \Delta$, this occurs when

$$\epsilon = \frac{\sqrt{\pi}}{8}(4 - \sqrt{2}) \approx 0.572. \tag{3.24}$$

The quantity given by (3.23) is related to the ratio of the nonlinear to dispersive terms in (2.15). That is, we define the following non-dimensional quantity as a measure of packet dynamics in the MNLSE,

$$\kappa = \frac{\epsilon^2(1 + b_0\Delta)}{\Delta^2}, \tag{3.25}$$

https://doi.org/10.1017/jfm.2019.428 Published online by Cambridge University Press

for b_0 a scaling constant. This is an extension of the parameter considered in Anderson (1983), as well as the so-called Benjamin–Feir index used in statistical studies of water waves (Alber 1978; Onorato *et al.* 2001; Janssen 2003).

Next, the minimum value of w, which we denote w_*, may be found explicitly by solving for $\Pi(w_*) = 0$, which implies

$$w_* = \frac{\sqrt{2\pi}\gamma_0 - \sqrt{8\pi\gamma_0^2 - 4(4\sqrt{\pi} - 4\alpha_0)(4\alpha_0 + 2\sqrt{2\pi}\gamma_0 - 4\sqrt{\pi} - C^2\sqrt{\pi})}}{4\alpha_0 - \sqrt{\pi}(4 + C^2 - 2\sqrt{2}\gamma_0)}. \tag{3.26}$$

Furthermore, it may be seen that $w \to 0$ for finite χ, as $\Pi(w) \to -\infty$ as $w \to 0$ when $\epsilon^2/\Delta \geqslant \sqrt{\pi}/2$. However, we are not explicitly interested in solutions that 'blow up' (Sulem & Sulem 1999), nor are we implying that these types of solutions exist in the MNLSE. Instead, we are interested in scenarios where A and its gradients become large (corresponding to large gradients in the free surface displacement η), hinting at the possibility of wave breaking in the more general water wave system where higher-order instabilities (e.g. five wave resonance) become operative and may quickly lead to wave overturning and breaking. To gain more intuition, we next numerically integrate the MNLSE.

3.3. *Numerical simulations of the MNLSE*

To better understand these predictions, we now look at several numerical examples. The numerical scheme is a split-step pseudo-spectral method, where the step size is chosen so that the energy is conserved to at least 1 part in 10^6 and the mean frequency to 1 part in 10^4. The number of modes was increased until convergence was found. In particular, we use 2^{12} modes and step sizes of the order of 10^{-5}.

Note, one of the difficulties in applying ideas from weakly nonlinear narrow banded theory to areas outside of their strict asymptotic region of validity is the choice in defining the (small) parameters ϵ and Δ (see the discussion in § 2 of Perlin *et al.* (2013)). For example, does one define the parameter ϵ as the initial slope, or the largest slope, as predicted by some theory? A technique used in laboratory experiments is to characterize the packet slope S based on the linear prediction of the maximum slope at focusing. This has been shown to be effective in describing the strength of breaking waves for laboratory wave packets (Drazen *et al.* 2008), which, due to wave channel length limitations, must be broadband in order to start as linear waves and progress to breaking over a reasonable fetch (usually on the order of 10 m). Based on this, we connect the parameters (ϵ, Δ) with the predictions of the maximum modulations to amplitude and spatial/temporal scales according to linear theory.

Figure 3 shows a comparison of the predictions of the trial functions with the MNLSE. Here, $\epsilon = \Delta = 0.1$. We can see good agreement between the predictions of the amplitude $|A|$ and the trial function amplitude $\mathcal{A} = |\mathcal{A}|e^{i\vartheta}$, while the frequency evolution θ_τ (where we recall $A = |A|e^{i\theta}$) agrees with trial function predictions until focusing, when the τ structure is more complicated than the low-order polynomials we assumed for ϑ. The lowest row shows the predictions of the magnitude of the envelope slope $|A_\tau|$ of the envelope during focusing, and there is relatively good agreement for small values of χ. However, this simple model is unable to predict the slope at focusing, as the asymmetric term is not part of the energy balance to this order and grows secularly.

https://doi.org/10.1017/jfm.2019.428 Published online by Cambridge University Press

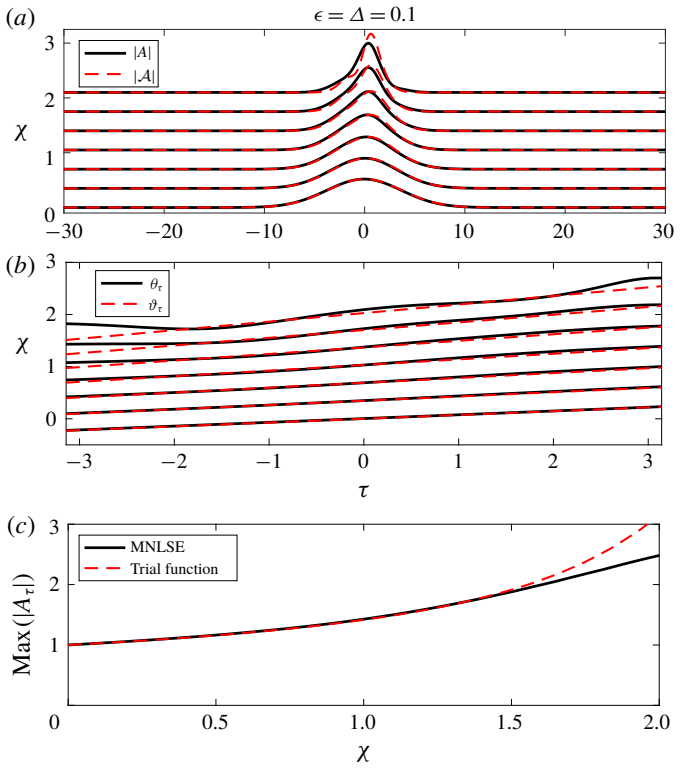


FIGURE 3. (Colour online) A comparison between numerical simulations of the MNLSE and the predictions of the trial function given by (3.3). Here, $\epsilon = \Delta = 0.1$. The envelope amplitude is shown in (*a*), where we see agreement between the trial function and the full solutions during focusing, with the agreement breaking down as the packet slope becomes large. The frequencies are shown in (*b*), and again the trial functions describe the bulk scale evolution of the phase but do not capture the higher τ-dependent behaviour. (*c*) Compares the predictions of the slope of the trial function and the MNLSE, with good agreement found for small values of χ, before the approximation breaks down.

3.4. *Maximum slope at focusing*

In this section we seek to model the maximum slope at focusing, based on the initial packet parameters (ϵ, Δ). The variational method hinted at the importance of $\gamma_0, \alpha_0, \beta_0$ in describing the focusing event. In particular, the values of w_*, which we recall is the minimum packet width predicted by the variational method, sets the scale of the envelope at focusing. These values are not uniquely defined as a function of ϵ, Δ, and to first order in ϵ^2/Δ, it may be seen that when $\Delta = d_0\epsilon + d_1\epsilon^2$, then lines of constant w_* may be found for $d_0^2/2 = w_*(1 - w_*)/(4w_*^2 - 2)$ and d_1 a more complicated function of w_* which is not presented here as it is not relevant for the ensuing discussion. This hints at a quasi self-similarity in the focusing event.

Next, the free surface η is given by (2.7). To better understand the dependence of $\max(|\eta_x|)$ on (ϵ, Δ), the MNLSE was numerically integrated with the initial conditions given by (3.1) for 400 values of ϵ and Δ, and the maximum of the modulus of the slope is shown in figure 4. Note, the three decibel width of the initial spectrum is chosen as a measure of the packet bandwidth, Δ. For comparison, the

https://doi.org/10.1017/jfm.2019.428 Published online by Cambridge University Press

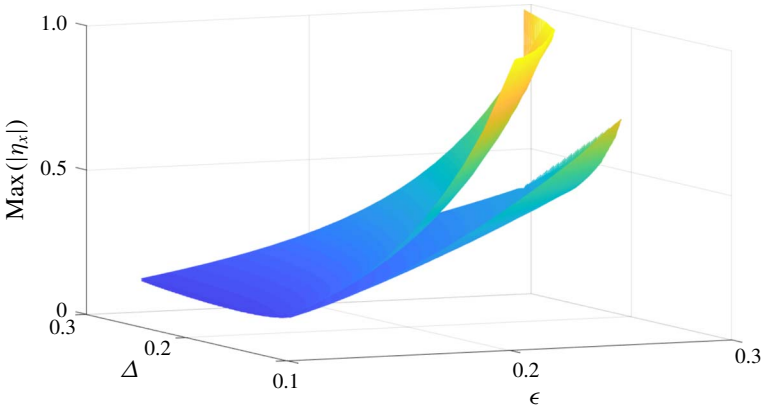


FIGURE 4. (Colour online) The maximum of the modulus of the slope, $\max(|\eta_x|)$, according to the modified nonlinear Schrodinger equation (upper surface) and nonlinear Schrodinger equation (lower surface) as a function of ϵ and Δ. Here, 400 runs were conducted, and the displayed surfaces are interpolated based on these data points. Note, the MNLSE predicts noticeably larger slopes than its lower-order counterpart, in accordance with the theoretical considerations of § 3. Slopes are largest for large ϵ and small Δ, corresponding to larger values of $\gamma_0, \alpha_0, \beta_0$.

same simulations are conducted for the NLSE and are shown. The slope predictions are larger for the MNLSE, and this becomes more pronounced with increasing ϵ and decreasing Δ (which corresponds to increasing $\gamma_0, \alpha_0, \beta_0$).

We define the maximum of the modulus of the free surface slope as $\mathcal{T}$, that is

$$\mathcal{T} \equiv \max(|\eta_x|). \tag{3.27}$$

For linear waves, we have $\mathcal{T} = \epsilon$, by definition. From (3.26), the definition of η (i.e. (2.7)), and the asymptotic self-similarity of w_* described above, we propose that for the MNLSE

$$\mathcal{T} = \epsilon(1 + f(\kappa)), \tag{3.28}$$

with κ as defined in (3.25) and f a function, to be constrained by the numerical simulations.

Next, by inspection of figure 4 we expect the growth of the slope to be sensitive to values of γ_0 and α_0. To this end, we assume that the function f is exponential, and find the following fit

$$\mathcal{T} = \epsilon \left(h_0 + h_1 \mathrm{e}^{h_2 \epsilon^2 / \Delta^2 (1 + h_3 \Delta)} \right), \tag{3.29}$$

with $(h_0, h_1, h_2, h_3) = (-0.37, 1.18, 0.20, 10.05)$ given by a least squares fit with the data. A comparison of this model with the data is shown in figure 5 in the form of a contour plot. There, bulk scale agreement between this simple model and the data is shown. Note, these coefficients also have a dependence on the chirp of the packet C.

Finally, note that (3.29) implies

$$\Delta = \frac{h_2 h_3 \epsilon^2 + \sqrt{h_2}\epsilon \sqrt{4 \ln(\mathcal{T}/\epsilon - h_0) + h_2 h_3^2 \epsilon^2 - 4 \ln(h_1)}}{2 \ln(\mathcal{T}/\epsilon - h_0) - 2 \ln(h_1)}. \tag{3.30}$$

https://doi.org/10.1017/jfm.2019.428 Published online by Cambridge University Press

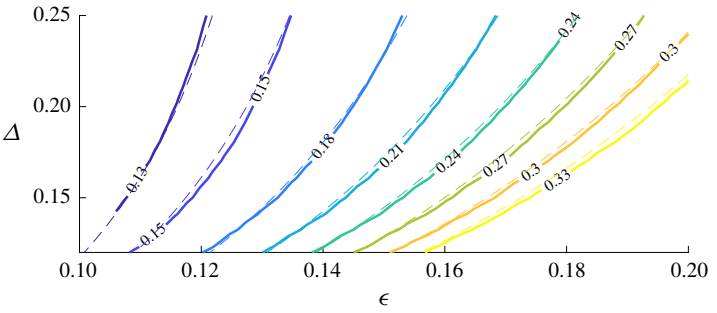


FIGURE 5. (Colour online) A comparison of the contours of $\max(|\eta_x|)$ as a function of (ϵ, Δ), with the model $\mathcal{T}$ (dashed lines) given by (3.29). There is a bulk scale agreement between this relatively simple model and the numerical simulations.

4. Numerical simulations of the fully nonlinear potential flow equations

Motivated by the quasi-self-similarity of focusing in the MNLSE, as well as the success of a simple model in predicting the maximum slope, we now investigate whether or not this may form a breaking criterion. That is, we assume all waves with a local slope that exceed some threshold $\mathcal{T}_0$ break. Specifically, we investigate how well a model of the form given by (3.30) partitions phase space between breaking and non-breaking waves.

To this end, we numerically integrate the equations of motion for fully nonlinear irrotational inviscid deep-water surface gravity waves. The numerical scheme of Dold & Peregrine (1986) is used (see also Dold 1992) to study focusing wave packets. This scheme iteratively solves Laplace's equation by using Cauchy's integral theorem. Initially, 2^{11} Lagrangian surface points are distributed along the free surface. Near the focusing point the system is remapped using a conformal mapping technique to increase resolution in this region (Boyd 2001), following similar techniques used in theoretical and numerical studies of Stokes waves (Yamada 1957; Tanaka 1983; Lushnikov, Dyachenko & Silantyev 2017). In particular, we map our horizontal domain to a unit circle. Then, if the original unit circle was described by $z = \mathrm{e}^{\mathrm{i}\zeta}$, the mapped points are given by $Z = \mathrm{e}^{\mathrm{i}\Theta}$, where

$$\Theta = \frac{\zeta + \nu_0}{1 + \nu_0 \zeta}; \quad -1 < \nu_0 \leqslant 0, \tag{4.1}$$

where ν_0 is a parameter prescribing how much to contract the region near $\zeta = \pi$ and stretch near $\zeta = 0$. We may shift this region to coincide with areas of maximum steepness, hence increasing the resolution in this region. We may also apply this mapping iteratively, to capture the fine scale structure of the free surface geometry near breaking. An example of this is shown in the inset of figure 6.

Our general numerical program is to run each simulation until the free surface curvature exceeds a threshold value, which is an indication that breaking might be occurring. Each simulation, regardless of whether or not breaking was suspected, is then rerun, starting one wave period before the largest magnitude of the observed slope. The mapping, i.e. equation (4.1), is then applied. We subsequently examined whether or not a wave in the packet has broken, where we say a wave has broken if the free surface becomes multivalued. Furthermore, we ensure that the total energy is conserved in this mapping to at least one part in 10^6.

https://doi.org/10.1017/jfm.2019.428 Published online by Cambridge University Press

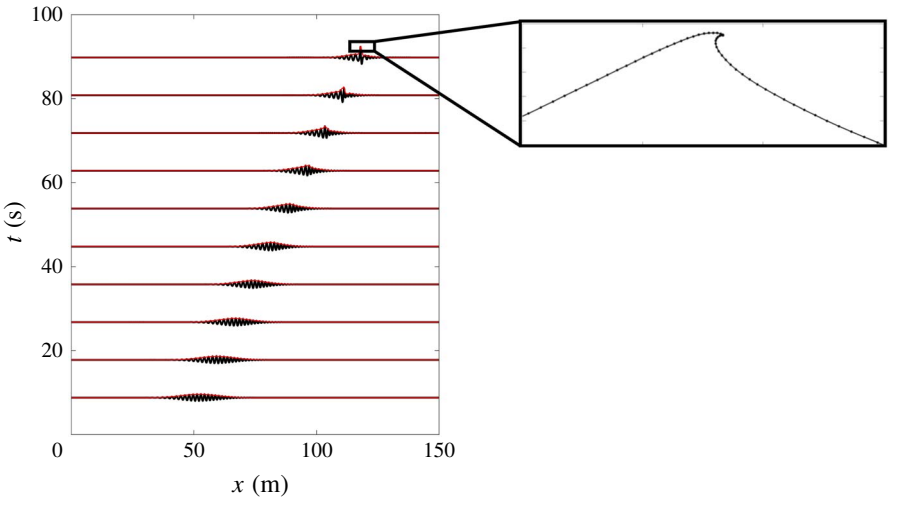


FIGURE 6. (Colour online) The packet evolution in the numerical simulations of the fully nonlinear potential flow equations, for $\epsilon = 0.18$ and $\Delta = 0.24$. A chirped packet uses dispersive focusing, so that longer faster waves catch up to shorter slower waves, leading to energy localization and in this case wave breaking. The free surface displacement η is shown black, while the packet envelope is shown in red. Note the asymmetric self-steepening on the forward face of the envelope and the amplitude amplification. The inset shows the breaking event after the particle locations have been remapped, with the particle locations shown by the black dots.

This technique allows us to create a numerical wave tank that resolves the jet of the breaking wave, and gives us the ability to accurately compute the geometry and kinematics of these waves at breaking. This offers significant advantages over large eddy simulations (Derakhti & Kirby 2016; Derakhti, Banner & Kirby 2018) which accurately capture post breaking bulk scale quantities and offer an insightful tool to study these integral properties, but suffer from poor resolution of the geometry of the free surface near breaking and hence also the free surface kinematics (Pizzo 2017).

As our initial conditions, following laboratory studies (Longuet-Higgins 1974; Rapp & Melville 1990), we use a dispersive focusing technique to localize energy density in space and time, possibly leading to wave breaking. These packets allow for future comparison with laboratory data, and enables us to test how well the predictions made in § 3 work for wave packets that are not explicitly chirped Gaussian packets.

The wave packets are of the form

$$\eta = \sum_{n=1}^{N} a_n \cos(k_n(x - x_b) - \omega_n(t - t_b)), \tag{4.2}$$

where N is the number of waves, taken to be 32 here (Drazen *et al.* 2008), x_b and t_b are the distance and time to focusing, with $t_b = c_g^{-1} x_b$, while ω_n and k_n are the frequency and wavenumber for each component, connected via the linear dispersion relationship $\omega_n^2 = g k_n$. The wavenumbers are chosen so that $k_n = k_0(1 + \delta(n-1)/N)$ for δ a constant related to the packet bandwidth.

https://doi.org/10.1017/jfm.2019.428 Published online by Cambridge University Press

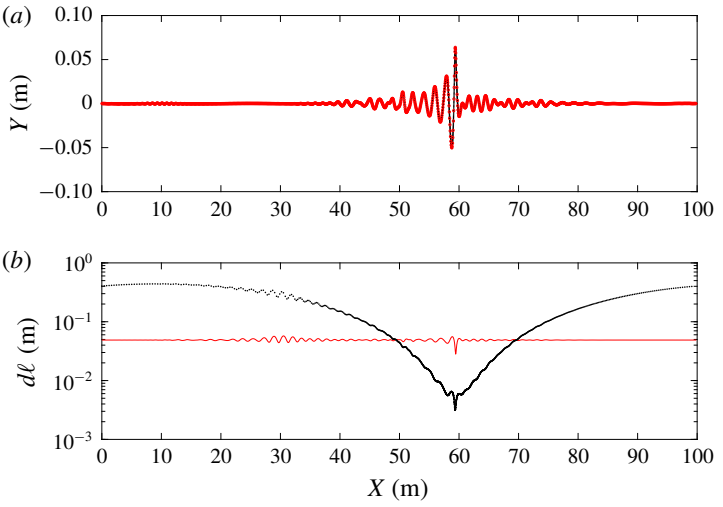


FIGURE 7. (Colour online) (*a*) The particle locations in the original integration are shown in red, while the mapped particle locations are shown in black. Here, $\nu_0 = -0.5$ in the conformal mapping given by (4.1)). The distance between adjacent particles in the original scheme (red) and the mapped coordinates (black). The resolution has been increased by nearly an order of magnitude near the steepest part of the wave using this technique.

Two parameters describe these wave packets. First, the linear prediction of the maximum slope at breaking is given by

$$S = \sum_{n=1}^{N} a_n k_n. \tag{4.3}$$

Next, the packet bandwidth is set by the parameter δ, as well as a windowing function that ensures that just one (initially compact) wave packet is generated (Rapp & Melville 1990). The three decibel width of the initial spectrum is chosen as a measure of the packet bandwidth, Δ. The distance to breaking, x_b is chosen so that $x_b = 5(\delta k_0)^{-1}$ which ensures that the original packet is linear (and the bound component contributions are initially negligible) and we take $f_0 = 1$ Hz.

An example of packet evolution in these numerical integrations is shown in figure 6. The black lines show the free surface elevation, while the red lines show the wave envelope evolution, found via the Hilbert transform (Melville 1983). The focusing process is marked by a strong asymmetric self-steepening on the forward face of the packet, eventually leading to wave breaking, which is shown in the figure inset.

Near focusing, the particle locations are remapped using (4.1), so that they become more dense in the region of largest slope magnitude. This is shown in figure 7. In figure 7(*a*), the original mapping is shown in red, while the re-mapped particles are shown in black, where ν_0 was taken to be -0.5. The distance between adjacent particles, $d\ell$, is then shown in figure 7(*b*) where it is seen that the resolution is enhanced by nearly an order of magnitude in this focusing region. This allows us to accurately capture the free surface geometry, which is crucial for detecting wave breaking.

We now perform 80 integrations of different initial conditions exploring the (ϵ, Δ) phase space, where following the above discussion we take ϵ to be S, the linear

https://doi.org/10.1017/jfm.2019.428 Published online by Cambridge University Press

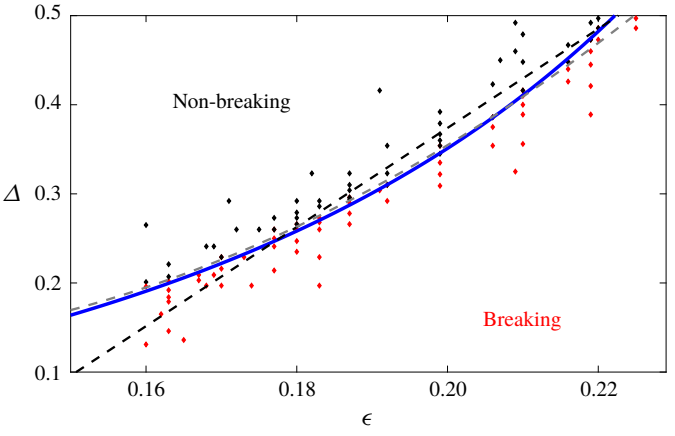


FIGURE 8. (Colour online) Top: numerical simulations of various initial bandwidths, Δ, and linear predictions of the maximum slope at focusing, ϵ. Red circles are wave packets with breaking, while those in black are wave packets where no breaking was observed. There is a distinct partitioning of this phase space between these two types of evolution. The model given by (4.4) is shown by the blue line, and describes the bulk scale partitioning of phase space between breaking and non-breaking waves, while the black line is a linear best to the data and the grey line shows the best fit to a quadratic polynomial in ϵ.

prediction of the maximum slope at focusing. The phase space is partitioned between breaking and non-breaking waves, as is shown in figure 8. We plot

$$\Delta = \xi_0 \frac{h_3 h_4 \epsilon^2 + \sqrt{h_3}\epsilon\sqrt{4\ln(\mathcal{T}/\epsilon - h_0) + h_3 h_4^2 \epsilon^2 - 4\ln(h_1)}}{2\ln(\mathcal{T}/\epsilon - h_0) - 2\ln(h_1)}, \tag{4.4}$$

where ξ_0 is best fit to the data with value 1.28. The blue line shows the prediction of our model with $\mathcal{T} = 0.28$, while the black dashed line shows a linear best fit to the data and the grey line shows the best fit of the data to a quadratic function.

We notice bulk scale agreement between the model and the numerical simulations. For larger values of ϵ and Δ the fit breaks down, as higher-order descriptions are needed to accurately predict the local slope (cf. (2.7)). Furthermore, the fine scale partitioning is not captured. Nevertheless, the bulk scale behaviour appears to be quasi-self-similar, and the models serves as a simple coarse description of the partitioning in phase space of breaking and non-breaking focusing chirped wave packets.

5. Conclusion

Near the peak of the spectrum, it is believed that wave–wave interactions are an important cause of wave breaking (Rapp & Melville 1990). Therefore, the chirped packets considered here serve as a model of these types of breaking events, highlighting the importance of the entire group structure in determining whether or not a wave breaks. This simple description of breaking may be used in more sophisticated statistical models of wave field evolution, where a local estimate of wave slope and bandwidth may be used together with the criterion given by (4.4) to quantify the breaking statistics. Coupled with recent field measurements of these breaking statistics

https://doi.org/10.1017/jfm.2019.428 Published online by Cambridge University Press

(Sutherland & Melville 2013, 2015), this may serve as an important constraint on models of the statistics of the surface wave field. Furthermore, this result may then be included in scaling arguments describing the breaking induced flow (e.g. the energy dissipation (Drazen *et al.* 2008), the circulation induced by breaking (Pizzo & Melville 2013) and the mass transport induced by breaking (Deike, Pizzo & Melville 2017; Pizzo, Melville & Deike 2019) to better describe the observations.

Despite the limitations of using a weakly nonlinear narrow-banded waves to examine wave breaking in deep-water surface gravity waves, the way to interpret the model presented in this paper is that it provides a simple qualitative description of the physics that can lead an initially symmetric wave packet up to the point where large gradients are expected in the free surface displacement, and breaking is likely. The results are studied numerically, and there is a bulk scale partitioning of phase space between non-breaking and breaking waves, which may be described by a model motivated by analysis of the quasi self-similarity found in focusing wave packets governed by the MNLSE.

Acknowledgement

This research was supported by grants to W.K.M. from the National Science Foundation (Physical Oceanography) and the Office of Naval Research. N.P. thanks the Kavli Institute for Theoretical Physics (supported by the National Science Foundation under grant no. NSF PHY17-48958), where part of this research was conducted. We also thank four anonymous referees, whose comments have led to significant improvements to the manuscript.

REFERENCES

AGRAWAL, G. P. 2007 *Nonlinear Fiber Optics*. Academic Press.

AKYLAS, T. R. 1989 Higher-order modulation effects on solitary wave envelopes in deep water. *J. Fluid Mech.* **198**, 387–397.

ALBER, I. E. 1978 The effects of randomness on the stability of two-dimensional surface wavetrains. *Proc. R. Soc. Lond.* A **363** (1715), 525–546.

ANDERSON, D. 1983 Variational approach to nonlinear pulse propagation in optical fibers. *Phys. Rev.* A **27** (6), 3135–3145.

BARTHELEMY, X., BANNER, M. L., PEIRSON, W. L., FEDELE, F., ALLIS, M. & DIAS, F. 2018 On a unified breaking onset threshold for gravity waves in deep and intermediate depth water. *J. Fluid Mech.* **841**, 463–488.

BENJAMIN, T. B. & FEIR, J. E. 1967 The disintegration of wave trains on deep water part 1. Theory. *J. Fluid Mech.* **27** (03), 417–430.

BOYD, J. P. 2001 *Chebyshev and Fourier Spectral Methods*. Courier Corporation.

BRIDGES, T. J. 2004 Superharmonic instability, homoclinic torus bifurcation and water-wave breaking. *J. Fluid Mech.* **505**, 153–162.

CAMASSA, R. & HOLM, D. D. 1993 An integrable shallow water equation with peaked solitons. *Phys. Rev. Lett.* **71** (11), 1661.

CAVALERI, L., FOX-KEMPER, B. & HEMER, M. 2012 Wind waves in the coupled climate system. *Bull. Am. Meteorol. Soc.* **93** (11), 1651–1661.

CHANDRASEKHAR, S. 2013 *Hydrodynamic and Hydromagnetic Stability*. Courier Corporation.

CHU, V. H. & MEI, C. C. 1970 On slowly-varying Stokes waves. *J. Fluid Mech.* **41** (04), 873–887.

CLAMOND, D., FRANCIUS, M., GRUE, J. & KHARIF, C. 2006 Long time interaction of envelope solitons and freak wave formations. *Eur. J. Mech. (B/Fluids)* **25** (5), 536–553.

CRAIK, A. D. D. 2005 George Gabriel stokes on water wave theory. *Annu. Rev. Fluid Mech.* **37**, 23–42.

https://doi.org/10.1017/jfm.2019.428 Published online by Cambridge University Press

DEIKE, L., MELVILLE, W. K. & POPINET, S. 2016 Air entrainment and bubble statistics in breaking waves. *J. Fluid Mech.* **801**, 91–129.

DEIKE, L., PIZZO, N. E. & MELVILLE, W. K. 2017 Lagrangian transport by breaking surface waves. *J. Fluid Mech.* **829**, 364–391.

DEIKE, L., POPINET, S. & MELVILLE, W. K. 2015 Capillary effects on wave breaking. *J. Fluid Mech.* **769**, 541–569.

DERAKHTI, M., BANNER, M. L. & KIRBY, J. T. 2018 Predicting the breaking strength of gravity water waves in deep and intermediate depth. *J. Fluid Mech.* **848**, R2-1–R2-12.

DERAKHTI, M. & KIRBY, J. T. 2016 Breaking-onset, energy and momentum flux in unsteady focused wave packets. *J. Fluid Mech.* **790**, 553–581.

DOLD, J. W. 1992 An efficient surface-integral algorithm applied to unsteady gravity waves. *J. Comput. Phys.* **103** (1), 90–115.

DOLD, J. W. & PEREGRINE, D. H. 1986 Water-wave modulation. *Coast. Engng Proc.* **1** (20), 671–679.

DRAZEN, D. A., MELVILLE, W. K. & LENAIN, L. 2008 Inertial scaling of dissipation in unsteady breaking waves. *J. Fluid Mech.* **611**, 307–332.

DUNCAN, J. H. 1981 An experimental investigation of breaking waves produced by a towed hydrofoil. *Proc. R. Soc. Lond.* A **377** (1770), 331–348.

DYACHENKO, A. I., KACHULIN, D. I. & ZAKHAROV, V. E. 2017 Super compact equation for water waves. *J. Fluid Mech.* **828**, 661–679.

DYACHENKO, A. I. & ZAKHAROV, V. E. 2011 Compact equation for gravity waves on deep water. *JETP Lett.* **93** (12), 701.

DYSTHE, K. B. 1979 Note on a modification to the nonlinear Schrödinger equation for application to deep water waves. *Proc. R. Soc. Lond.* A **369** (1736), 105–114.

FEDELE, F. 2014 On certain properties of the compact Zakharov equation. *J. Fluid Mech.* **748**, 692–711.

GRAMSTAD, O. & TRULSEN, K. 2011 Hamiltonian form of the modified nonlinear Schrödinger equation for gravity waves on arbitrary depth. *J. Fluid Mech.* **670**, 404–426.

JANSSEN, P. A. E. M. 1983 On a fourth-order envelope equation for deep-water waves. *J. Fluid Mech.* **126**, 1–11.

JANSSEN, P. A. E. M. 2003 Nonlinear four-wave interactions and freak waves. *J. Phys. Oceanogr.* **33** (4), 863–884.

KHAIT, A. & SHEMER, L. 2018 On the kinematic criterion for the inception of breaking in surface gravity waves: fully nonlinear numerical simulations and experimental verification. *Phys. Fluids* **30** (5), 057103.

KIT, E. & SHEMER, L. 2002 Spatial versions of the Zakharov and Dysthe evolution equations for deep-water gravity waves. *J. Fluid Mech.* **450**, 201–205.

LO, E. & MEI, C. C. 1985 A numerical study of water-wave modulation based on a higher-order nonlinear Schrödinger equation. *J. Fluid Mech.* **150**, 395–416.

LONGUET-HIGGINS, M. S. 1974 Breaking waves in deep or shallow water. In *Proceedings of the 10th Conference on Naval Hydrodynamics*, vol. 597. Massachusetts Institute of Technology.

LONGUET-HIGGINS, M. S. 1978 The instabilities of gravity waves of finite amplitude in deep water. I. Superharmonics. *Proc. R. Soc. Lond.* A **360** (1703), 471–488.

LONGUET-HIGGINS, M. S. & DOMMERMUTH, D. G. 1997 Crest instabilities of gravity waves. Part 3. Nonlinear development and breaking. *J. Fluid Mech.* **336**, 33–50.

LONGUET-HIGGINS, M. S. & STEWART, R. W. 1964 Radiation stresses in water waves; a physical discussion, with applications. *Deep-Sea Res. Oceanogr. Abstracts* **11** (4), 529–562.

LUKE, J. C. 1967 A variational principle for a fluid with a free surface. *J. Fluid Mech.* **27** (02), 395–397.

LUSHNIKOV, P. M., DYACHENKO, S. A. & SILANTYEV, D. A. 2017 New conformal mapping for adaptive resolving of the complex singularities of Stokes wave. *Proc. R. Soc. Lond.* A **473** (2202), 20170198.

MCINTYRE, M. E. 1981 On the wave momentum myth. *J. Fluid Mech.* **106**, 331–347.

https://doi.org/10.1017/jfm.2019.428 Published online by Cambridge University Press

McLean, J. W., Ma, Y. C., Martin, D. U., Saffman, P. G. & Yuen, H. C. 1981 Three-dimensional instability of finite-amplitude water waves. *Phys. Rev. Lett.* **46** (13), 817.

Melville, W. K. 1982 The instability and breaking of deep-water waves. *J. Fluid Mech.* **115**, 165–185.

Melville, W. K. 1983 Wave modulation and breakdown. *J. Fluid Mech.* **128**, 489–506.

Melville, W. K. 1996 The role of surface wave breaking in air–sea interaction. *Annu. Rev. Fluid Mech.* **28**, 279–321.

Melville, W. K. & Rapp, R. J. 1985 Momentum flux in breaking waves. *Nature* **317** (6037), 514–516.

Miles, J. W. 1977 On Hamilton's principle for surface waves. *J. Fluid Mech.* **83** (01), 153–158.

Onorato, M., Osborne, A. R., Serio, M. & Bertone, S. 2001 Freak waves in random oceanic sea states. *Phys. Rev. Lett.* **86** (25), 5831.

Perlin, M., Choi, W. & Tian, Z. 2013 Breaking waves in deep and intermediate waters. *Annu. Rev. Fluid Mech.* **45**, 115–145.

Phillips, O. M. 1977 *The Dynamics of The Upper Ocean*. Cambridge University Press.

Phillips, O. M. 1981 Wave interactions-the evolution of an idea. *J. Fluid Mech.* **106**, 215–227.

Phillips, O. M. 1985 Spectral and statistical properties of the equilibrium range in wind-generated gravity waves. *J. Fluid Mech.* **156** (1), 505–531.

Pizzo, N. E. 2017 Surfing surface gravity waves. *J. Fluid Mech.* **823**, 316–328.

Pizzo, N. E. & Melville, W. K. 2013 Vortex generation by deep-water breaking waves. *J. Fluid Mech.* **734**, 198–218.

Pizzo, N. E. & Melville, W. K. 2016 Wave modulation: the geometry, kinematics, and dynamics of surface-wave packets. *J. Fluid Mech.* **803**, 275–291.

Pizzo, N. E., Melville, W. K. & Deike, L. 2016 Current generation by deep-water wave breaking. *J. Fluid Mech.* **803**, 292–312.

Pizzo, N. E., Melville, W. K. & Deike, L. 2019 Lagrangian transport by non-breaking and breaking deep-water waves at the ocean surface. *J. Phys. Oceanogr.* **49** (4), 983–992.

Pomeau, Y., Le Berre, M., Guyenne, P. & Grilli, S. 2008 Wave-breaking and generic singularities of nonlinear hyperbolic equations. *Nonlinearity* **21** (5), T61.

Rapp, R. J. & Melville, W. K. 1990 Laboratory measurements of deep-water breaking waves. *Phil. Trans. R. Soc. Lond.* A **331**, 735–800.

Romero, L., Melville, W. K. & Kleiss, J. M. 2012 Spectral energy dissipation due to surface wave breaking. *J. Phys. Oceanogr.* **42** (9), 1421–1444.

Saket, A., Peirson, W. L., Banner, M. L., Barthelemy, X. & Allis, M. J. 2017 On the threshold for wave breaking of two-dimensional deep water wave groups in the absence and presence of wind. *J. Fluid Mech.* **811**, 642–658.

Seliger, R. L. 1968 A note on the breaking of waves. *Proc. R. Soc. Lond.* A **303** (1475), 493–496.

Shemer, L., Kit, E. & Jiao, H. 2002 An experimental and numerical study of the spatial evolution of unidirectional nonlinear water-wave groups. *Phys. Fluids* **14** (10), 3380–3390.

Stokes, G. G. 1880 *On the Theory of Oscillatory Waves, Appendix B*. Cambridge University Press.

Sulem, C. & Sulem, P.-L. 1999 *The Nonlinear Schrödinger Equation: Self-Focusing and Wave Collapse*, vol. 139. Springer.

Sullivan, P. P., McWilliams, J. C. & Melville, W. K. 2007 Surface gravity wave effects in the oceanic boundary layer: large-eddy simulation with vortex force and stochastic breakers. *J. Fluid Mech.* **593**, 405–452.

Sutherland, P. & Melville, W. K. 2013 Field measurements and scaling of ocean surface wave-breaking statistics. *Geophys. Res. Lett.* **40** (12), 3074–3079.

Sutherland, P. & Melville, W. K. 2015 Field measurements of surface and near-surface turbulence in the presence of breaking waves. *J. Phys. Oceanogr.* **45** (4), 943–965.

Tanaka, M. 1983 The stability of steep gravity waves. *J. Phys. Soc. Japan* **52** (9), 3047–3055.

Temme, N. M. 2010 Error functions, Dawson's and Fresnel integrals. In *NIST Handbook of Mathematical Functions*, pp. 159–171. Cambridge University Press.

Tian, Z., Perlin, M. & Choi, W. 2010 Energy dissipation in two-dimensional unsteady plunging breakers and an eddy viscosity model. *J. Fluid Mech.* **655**, 217–257.

https://doi.org/10.1017/jfm.2019.428 Published online by Cambridge University Press

TITCHMARSH, E. C. 1948 *Introduction to the Theory of Fourier Integrals*. Clarendon Press.

TRULSEN, K. 2006 *Weakly Nonlinear and Stochastic Properties of Ocean Wave Fields. Application to An Extreme Wave Event*, Springer.

TRULSEN, K. & DYSTHE, K. B. 1997 Frequency downshift in three-dimensional wave trains in a deep basin. *J. Fluid Mech.* **352**, 359–373.

TRULSEN, K., KLIAKHANDLER, I., DYSTHE, K. B. & VELARDE, M. G. 2000 On weakly nonlinear modulation of waves on deep water. *Phys. Fluids* **12** (10), 2432–2437.

WHITHAM, G. B. 1965 A general approach to linear and non-linear dispersive waves using a Lagrangian. *J. Fluid Mech.* **22** (02), 273–283.

WHITHAM, G. B. 1974 *Linear and Nonlinear Waves*. Wiley.

YAMADA, H. 1957 Highest waves of permanent type on the surface of deep water. *Report Res. Inst. Appl. Mech. Kyushu Univ.* **5**, 37–52.

ZAKHAROV, V. E. 1968 Stability of periodic waves of finite amplitude on the surface of a deep fluid. *J. Appl. Mech. Tech. Phys.* **9** (2), 190–194.

https://doi.org/10.1017/jfm.2019.428 Published online by Cambridge University Press